

Dramatic visible photocatalytic performance of g-C₃N₄-based nanocomposite due to the synergistic effect of AgBr and ZnO semiconductors



Elham Boorboor Azimi^a, Alireza Badiei^{a,*}, Moayad Hossaini Sadr^b

^a School of Chemistry, College of Science, University of Tehran, Tehran, Iran

^b Chemistry Dept., Faculty of Science, Azarbaijan Shahid Madani University, Tabriz, Iran

ARTICLE INFO

Keywords:

Graphitic carbon nitride
Silver bromide
Zinc oxide
Methylene blue
Dye photosensitization

ABSTRACT

In this study, we synthesized a novel visible-light-driven photocatalyst with excellent photocatalytic activity, g-C₃N₄/AgBr/ZnO, as a ternary nanocomposite for pollutant degradation via a facile method. This coupling was favorable due to charge transfer between the semiconductors to yield a Z-scheme photocatalysis system, and thus the separation of photo-excited electron–holes was improved. The structure, morphology, and optical properties of the photocatalyst were determined by using characterization techniques, including X-ray diffraction, transmission electron microscopy, scanning electron microscopy with energy dispersive X-ray spectroscopy and its elemental mapping, N₂ adsorption-desorption analysis, ultraviolet-visible diffuse reflectance spectroscopy, photoluminescence, fourier transform infrared spectra, and zeta potential measurements. The photocatalytic activity of the g-C₃N₄/AgBr/ZnO heterostructure was evaluated with different weight ratios during the degradation of the cationic pollutant methylene blue (MB) under exposure to visible light. The optimal photocatalyst with a g-C₃N₄ content of 30% exhibited superior activity during the degradation of MB and the rate constant of 0.041 min⁻¹ was about 4.6 times higher than the rate constant of the pure g-C₃N₄. In addition, we assessed the photosensitization of MB and its effect on the photodegradation process. We propose a possible mechanism to explain the photocatalytic activity of the prepared ternary nanocomposite based on experiments with reactive species scavengers. Finally, the reusability and stability of the photocatalyst was investigated after four cycles.

1. Introduction

Increasing concerns about environmental issues have motivated researchers to identify suitable semiconductor photocatalysts for degrading pollutants [1–7]. The most widely investigated semiconductor is TiO₂ because it has many advantages as an excellent photocatalyst when exposed to ultraviolet (UV) light due to its wide band gap. Sunlight is the best energy source for solving environmental issues but only 4% of the sunlight is in the UV region and most of the solar spectrum lies in the visible region, so an ideal material should have a band gap that absorbs light in the visible range. In addition, it should be non-toxic, abundant, thermally and chemically stable, and inexpensive. Polymeric graphite-like carbon nitride (g-C₃N₄) has an appropriate optical band gap of 2.7 eV, and thus it has attracted much attention in recent years [8–14]. Despite these excellent features, g-C₃N₄ has a rapid recombination rate for photogenerated electrons and holes, which hinder its applications as a photocatalyst. Many attempts have been made to address this problem in order to enhance the photocatalytic activity of g-C₃N₄, including nanoporous structure design [15],

morphology control [16–18], doping with metal or non-metal ions such as Cu [19], V [20], Ag [21], B [22], P [23], and F [24], and coupling with other semiconductor materials with well-aligned band gaps such as TiO₂ [25], BiOX [26], AgX [27], BiVO₄ [28], Ag₂S [9], and some clusters [29]. These attempts to modify g-C₃N₄ with dopants created mid-gap states to increase the absorption of visible light, but these states could also act as recombination centers for photogenerated electron–hole pairs and decrease the photocatalytic efficiency. However, constructing a heterostructure by coupling g-C₃N₄ with other semiconductors may improve the separation of the photogenerated carriers and obtain higher photocatalytic performance.

In our previous studies, we prepared a new and improved photocatalyst with enhanced photocatalytic activity for degrading pollutants [30–34], where we employed silver bromide and zinc oxide to modify g-C₃N₄. Zinc oxide is of particular interest because its appropriate direct band gap of 3.03 eV, high electron mobility, and high redox potential make it a good photocatalyst [35]. However, ZnO cannot be applied under illumination with visible light. Silver bromide is a fascinating semiconductor with a band gap of about 2.5 eV and it can degrade

* Corresponding author.

E-mail address: abadiei@khayam.ut.ac.ir (A. Badiei).

pollutants under irradiation with visible light [36], but it is hindered by the rapid rate of recombination between electron and hole pairs. The locations of the conduction band (CB) and valence band (VB) in ZnO and AgBr make them highly suitable for combining with g-C₃N₄ to form a good heterojunction. To the best of our knowledge, no previous study has reported the use of a ternary g-C₃N₄/AgBr/ZnO nanocomposite as a photocatalyst. In order to assess the photocatalytic activity of this photocatalyst, we tested the photodegradation of methylene blue (MB) as an organic pollutant under irradiation with visible light. We explored the issue of catalyst photosensitization by MB by determining the changes in the UV-visible (UV-Vis) absorption spectra for MB during the photodegradation process [37]. Furthermore, we investigated whether the degradation of the dye was due to the photocatalytic activity of the photocatalyst or MB photosensitization.

2. Experimental section

2.1. Materials and methods

Potassium bromide and hydrogen chloride were purchased from Sigma-Aldrich and used without further purification. Silver nitrate, zinc nitrate hexahydrate, dicyandiamide, and sodium hydroxide were purchased from Merck and used without further purification. X-ray powder diffraction (XRD) was performed with a Bruker D8 Advance X-ray diffractometer (Philips, PW 1730, Netherland) with Cu K α radiation in the range of $2\theta = 10$ – 80° . Transmission electron microscopy (TEM) was conducted using a CM30 system with an accelerating voltage of 300 kV. Scanning electron microscopy (SEM) micrographs was prepared with a MIRA3, TESCAN instrument equipped with energy dispersive X-ray (EDX) and elemental mapping. UV-Vis diffuse reflectance spectroscopy (DRS) was performed with an AvaSpec-2048 TEC spectrometer. Photoluminescence (PL) spectra were recorded for the samples at room temperature using an Agilent-G980A instrument. Fourier transform infrared spectroscopy (FTIR) spectra were obtained for the samples using a RAYLEIGH WQF-510 A system in the wave number range of 4000–600 cm⁻¹. Zeta potentials were recorded with a Zetasizer (Nano ZS, Malvern, UK) at room temperature. The specific surface areas were estimated using the BET (Brunauer–Emmett–Teller) method, and the adsorption branch of isotherm based on the BJH (Barrett–Joyner–Halenda) model was used to calculate the pore size distributions. An ultrasonic bath was used to protonate g-C₃N₄.

2.2. Synthesis of g-C₃N₄ and protonation treatment

Bulk g-C₃N₄ was prepared by heating dicyandiamide as described previously [38]. First, 2 g of dicyandiamide was placed in a ceramic crucible and heated to 350 °C at a rate of 2.9 K min⁻¹, and kept at this temperature for 2 h in a flowing nitrogen atmosphere. Next, the product was heated at a rate of 3.3 K min⁻¹ to a temperature of 550 °C and held at this temperature for another 2 h in a flowing nitrogen atmosphere. The carbon nitride obtained was crushed into powder. An ultrasound bath was used to protonate the prepared graphitic carbon nitride, where 1.0 g of g-C₃N₄ was ultrasonicated in HCl (0.5 M, 200 mL) for 1 h, before magnetic stirring at room temperature for 4 h [39]. The protonated g-C₃N₄ was then washed with deionized water until neutral conditions and dried at 70 °C in air for 12 h. The protonated g-C₃N₄ was denoted as PCN.

2.3. Development of pg-C₃N₄/AgBr/ZnO (CN/AB/ZO) and pg-C₃N₄/AgBr (CN/AB)

The CN/AB/ZO samples were prepared via a sonication-assisted deposition-precipitation technique. Typically, 0.15 g of the PCN was added to 20 mL of ethanol and sonicated for 1 h. Next, a solution of KBr (0.374 g in 50 mL double distilled water) was added to the suspension in excess to ensure that the amount of halide ions from KBr was more

Table 1

Percentage compositions of the different weight ratios for the photocatalysts.

	g-C ₃ N ₄	AgBr	ZnO
CN	100	0	0
CN/AB	75.2	24.8	0
CN/AB/ZO 60	70.9	23.4	5.7
CN/AB/ZO 50	59.3	32.8	7.9
CN/AB/ZO 40	42.2	46.6	11.2
CN/AB/ZO 30	25.1	60.0	14.9
CN/AB/ZO 20	17.1	66.8	16.6

than sufficient to precipitate Ag⁺ on the g-C₃N₄ surface. The mixture was stirred magnetically for 1 h. An aqueous solution of AgNO₃ (0.32 g, 20 mL) was then added dropwise to the suspension. The dropwise addition of AgNO₃ was necessary to avoid the rapid nucleation process by Ag⁺ and Br⁻ on PCN in the solution. After stirring for 1 h at room temperature, we added 0.32 g of zinc nitrate hexahydrate dissolved in 20 mL double distilled water. The resulting mixture was stirred vigorously at room temperature for 3 h. An aqueous solution of NaOH (5 M) was then added dropwise to the solution under strong stirring at room temperature until the pH of the suspension reached 10. Subsequently, the suspension was refluxed for 3 h. The product obtained was filtered and the precipitate was washed with double distilled water and ethanol two times to remove the unreacted reagents, before drying in an oven at 60 °C for 24 h. Different weight ratios of g-C₃N₄ were obtained and designated as CN/AB/ZO x, where x is the approximate weight ratio of g-C₃N₄ relative to AgBr and ZnO in equal amounts. Thus, CN/AB/ZO 60, CN/AB/ZO 50, CN/AB/ZO 40, CN/AB/ZO 30, and CN/AB/ZO 20 nanocomposites were prepared in this manner. Table 1 shows the composition measured for each sample. For comparison, pg-C₃N₄/AgBr was prepared using the same procedure but without the addition of Zn (NO₃)₂·6H₂O and NaOH, where addition of AgNO₃ was followed by stirring for 3 h at room temperature, filtering the product, and washing with double distilled water and ethanol several times. The prepared sample was dried in an oven at 60C for 24 h. The product was designated as CN/AB.

2.4. Photocatalytic activity test

The prepared nanocomposites were tested by investigating the degradation of the organic dye MB at room temperature under irradiation with visible light provided by a 300 W halogen lamp (Osram), where a glass lid filtered wavelengths lower than 420 nm. First, the amount of photocatalyst was optimized for the degradation process. As shown in Fig. 1, 40 mg of the photocatalyst obtained the highest MB removal efficiency. In a typical photocatalytic experiment, the photocatalyst (0.04 g) was dispersed in MB solution (100 mL, 5.0 mg L⁻¹). Before illumination, the suspension was stirred magnetically in darkness for 30 min to ensure that the adsorption–desorption equilibrium was reached. At irradiation time intervals of 20 min, 4 mL of the suspension was collected and centrifuged for 10 min. The catalyst-free MB solution was then analyzed with a UV-Vis spectrophotometer (Raleigh UV-1600) at a wavelength of 665 nm with distilled water as a reference sample.

3. Results and discussion

3.1. Synthesis of CN/AB/ZO 30

The synthesis of the photocatalyst is shown schematically in Fig. 2. First, g-C₃N₄ was prepared from melamine. Next, it was protonated to increase its activity and then highly dispersed in water to react with other composites. KBr and AgNO₃ were used to form AgBr nanocomposites coupled with g-C₃N₄. Zn(NO₃)₂·6H₂O was added to form Zn²⁺ in the structure and the addition of NaOH made the solution alkaline, so ZnO nanocomposites formed in the structure of g-C₃N₄.

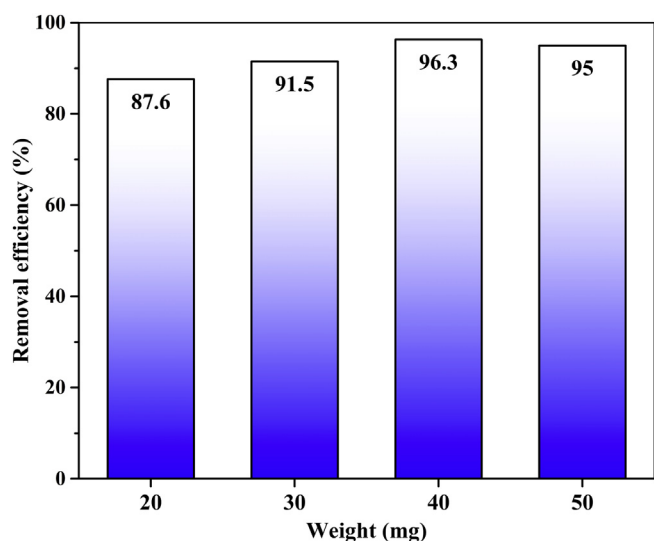


Fig. 1. Optimizing the amount of photocatalyst.

Finally, well-distributed ternary nanocomposites were synthesized.

3.2. XRD

XRD analysis was conducted to investigate the phase structures of $g\text{-C}_3\text{N}_4$, CN/AB, and CN/AB/ZO with different $g\text{-C}_3\text{N}_4$ contents. As shown in Fig. 3, the broad diffraction at $2\theta = 27.3$ could be indexed to the (002) plane of $g\text{-C}_3\text{N}_4$. In addition, the diffraction at 13° represented the in-plane structural packing motif of tri-*s*-triazine units indexed to the (100) plane [8]. The XRD pattern obtained for PCN was similar to that for pure $g\text{-C}_3\text{N}_4$, which indicated that after HCl treatment, the nature of $g\text{-C}_3\text{N}_4$ was unchanged in the PCN structure and the only chemical refinement was the increased activity. The diffractions at the 2θ values in the CN/AB pattern at 27° , 30.8° , 44.2° , 53° , 54.8° , 64.2° , and 73.2° were attributed to the (111), (200), (220), (311), (222), (400), and (420) lattice planes, respectively, of the AgBr cubic crystal [40]. The diffraction peaks at 31.4° , 34.0° , 36.0° , 47.8° , 56.3° , 62.6° , 67.8° , and 69.0° corresponded to the (100), (002), (101), (102), (110), (103), (112), and (201) crystalline planes of ZnO, respectively, which could be simply indexed to the hexagonal Wurtzite structure [41]. As the $g\text{-C}_3\text{N}_4$ content decreased in the photocatalyst from CN to CN/ZB/ZO 20, the

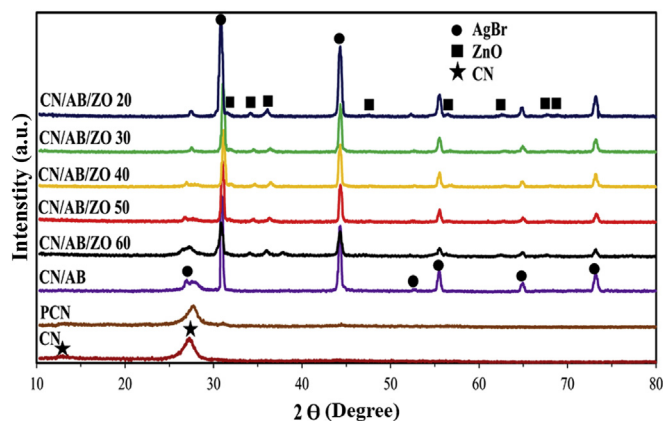


Fig. 3. XRD patterns obtained for $g\text{-C}_3\text{N}_4$, $g\text{-C}_3\text{N}_4/\text{AgBr}$, and $g\text{-C}_3\text{N}_4/\text{AgBr}/\text{ZnO}$ nanocomposites.

intensities of the diffraction peaks obtained for $g\text{-C}_3\text{N}_4$ also decreased, whereas those for AgBr and ZnO increased due to the higher amounts of AgBr and ZnO. In addition, the grain sizes of the $g\text{-C}_3\text{N}_4/\text{AgBr}/\text{ZnO}$ nanocomposites were obtained from the XRD results using the Scherrer equation [42]. Based on the calculations, the grain sizes of the AgBr nanocomposites were estimated at around 16–17 nm, and those for the ZnO nanocomposites were calculated at around 6.2 and 11.9 nm for the two planes.

3.3. SEM and TEM

As shown in Fig. 4, SEM and TEM images were acquired in order to investigate the morphology and microstructure of $g\text{-C}_3\text{N}_4$ and $g\text{-C}_3\text{N}_4/\text{AgBr}/\text{ZnO}$ 30. The SEM image of pure $g\text{-C}_3\text{N}_4$ (Fig. 4a) contained large clumps with an irregular morphology. After loading with AgBr and ZnO (Fig. 4b), the morphology changed greatly and most of the $g\text{-C}_3\text{N}_4$ surfaces were covered. The TEM image in Fig. 4c shows that pure $g\text{-C}_3\text{N}_4$ had a cloud-like structure. The well scattered anchoring of AgBr and ZnO on $g\text{-C}_3\text{N}_4$ is shown clearly in Fig. 4d, where a heterojunction formed between them. In addition, based on the size of the nanocomposites calculated based on the XRD results, the results for AgBr and ZnO are shown in the TEM image. In conclusion, according to the XRD patterns, the ternary nanocomposite $g\text{-C}_3\text{N}_4/\text{AgBr}/\text{ZnO}$ was produced successfully and a heterostructure formed between the

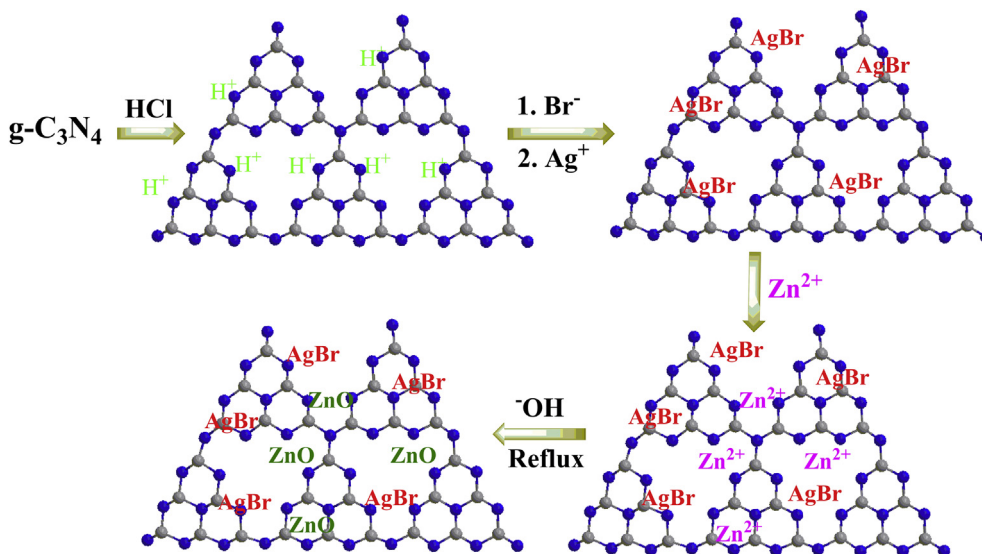


Fig. 2. Schematic illustrating the synthesis of CN/AB/ZO from $g\text{-C}_3\text{N}_4$.

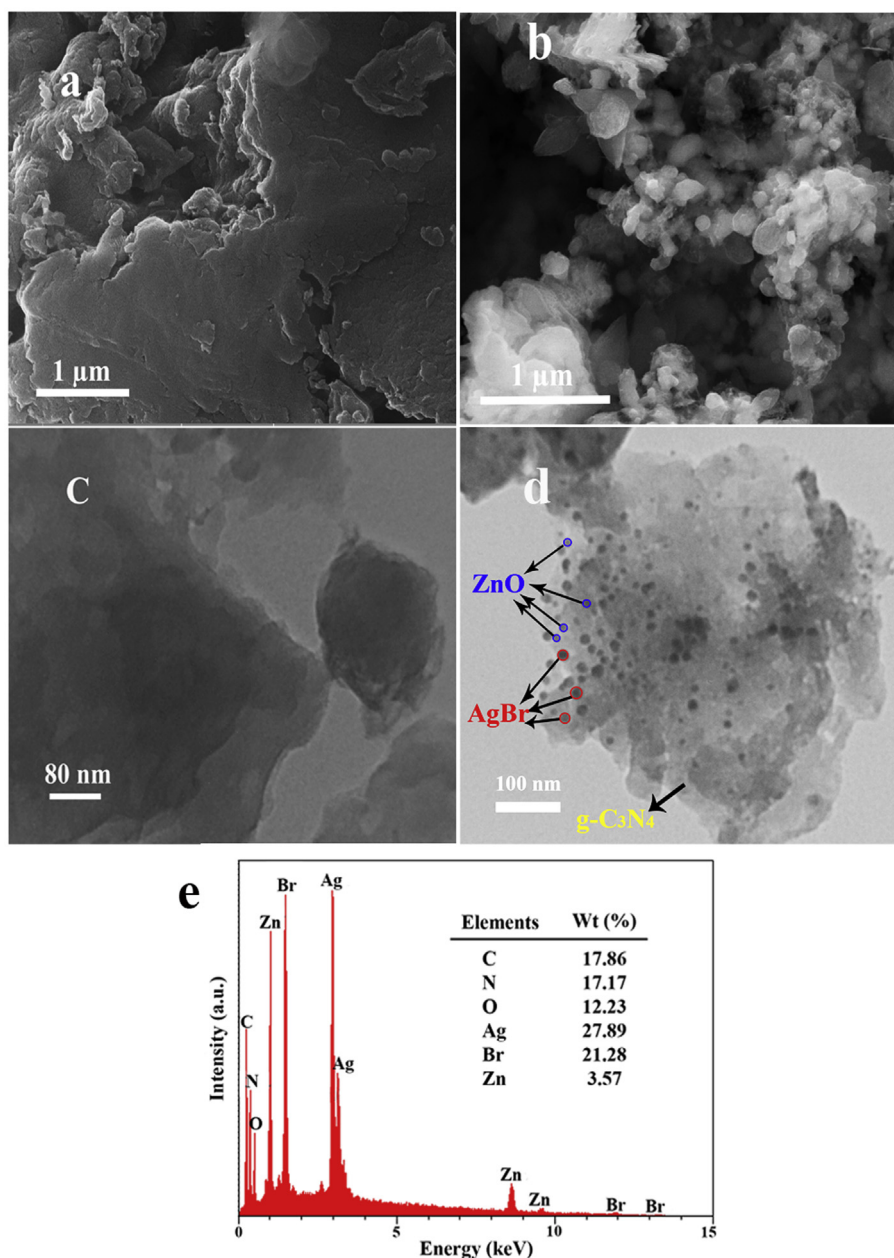


Fig. 4. SEM images of: (a) CN and (b) CN/AB/ZO 30; and TEM images of (c) CN and (d) CN/AB/ZO 30. (e) SEM-EDX spectra and elemental percentages in CN/AB/ZO 30.

semiconductors. The SEM-EDX results in Fig. 4e demonstrate the presence of Zn, Ag, Br, and O, as well as C and N elements. The weight percentage of the elements in CN/AB/ZO 30 showed that the nitrogen content decreased as the oxygen content increased, and to a much higher level than the zinc in zinc oxide, thereby indicating that the oxygen atoms could be substituted by nitrogen atoms. The elemental mapping of the optimized photocatalyst shown in Fig. 5 also indicates the presence of the elements, where all of the elements were distributed well in the structure of the ternary nanocomposite.

3.4. N_2 adsorption-desorption

The N_2 adsorption-desorption isotherms were generated in order to determine the specific surface area and pore distribution in $g-C_3N_4$ /AgBr/ZnO 30 compared with $g-C_3N_4$, as shown in Fig. 6. The N_2 adsorption-desorption isotherms were type IV isotherms, thereby indicating the mesoporous structure of the photocatalysts. The specific

surface area of the pure $g-C_3N_4$ was calculated as $11 \text{ m}^2 \text{ g}^{-1}$ and after modification with AgBr and ZnO, it reduced to $8 \text{ m}^2 \text{ g}^{-1}$. This decrease in the surface area could be attributed to reductions in the number of small pores, which was also verified by the pore size distribution curves (as shown in the inset in Fig. 6), where the total pore volumes were calculated as $0/029$ and $0/024 \text{ cm}^3 \text{ g}^{-1}$ for CN and CN/AB/ZO 30, respectively. These results demonstrate that the higher photocatalytic activity of the modified $g-C_3N_4$ was not due to a change in the surface area.

3.5. FTIR

Fig. 7 compares the FTIR spectra obtained for the pure $g-C_3N_4$, $g-C_3N_4$ /AgBr, and $g-C_3N_4$ /AgBr/ZnO nanocomposites with different weight ratios. The peaks at 1240, 1322, 1410, 1563, and 1634 cm^{-1} corresponded to the typical stretching vibration modes of C-N and C=N heterocycles [43]. Furthermore, the band at 808 cm^{-1} was related to

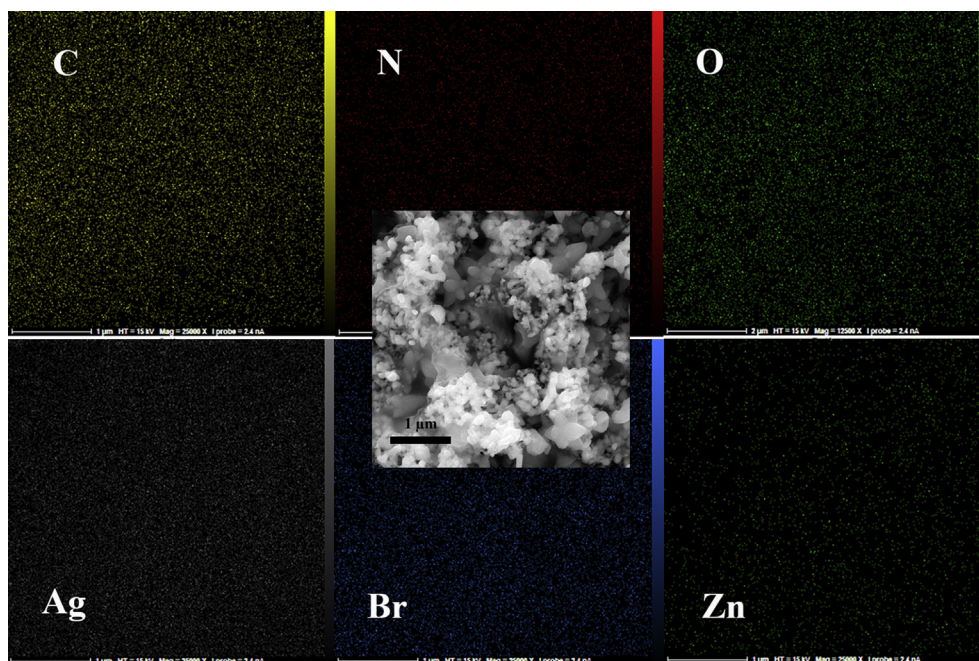
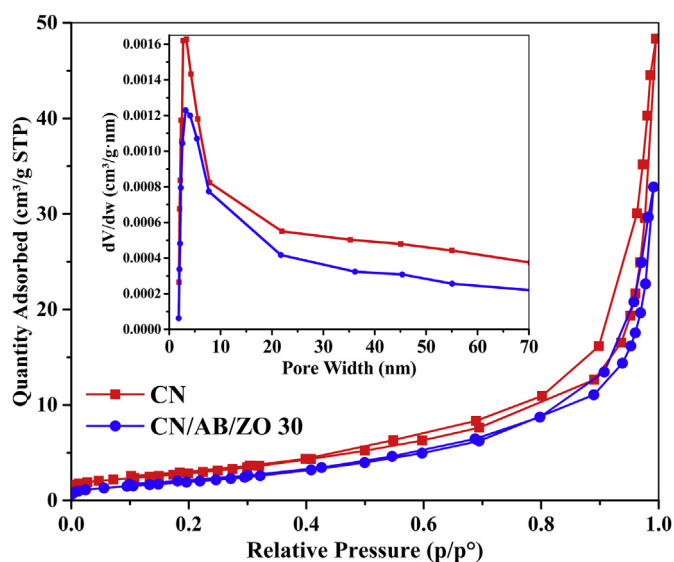


Fig. 5. Elemental mapping of CN/AB/ZO 30.

Fig. 6. N₂ adsorption–desorption isotherms and (inset) pore size distribution curves for the photocatalysts.

the breathing mode of the triazine units [44]. In all the samples, the wide absorption band at 3000–3300 cm⁻¹ was due to the terminal NH₂ or NH groups at defect sites in g-C₃N₄ aromatic rings [44]. However, this wide band was weaker in the CN/AB/ZO ternary nanocomposites, probable due to the lower amount of g-C₃N₄ and the reactions between amines and the composites. Clearly, the main characteristic peaks of g-C₃N₄ appeared in all of the photocatalysts. The modifications with AgBr and ZnO did not greatly modify the IR spectrum for g-C₃N₄, which indicates that FTIR was not sufficiently sensitive to study the interaction between AgBr/ZnO and g-C₃N₄. These results indicate that there were no covalent bonds between g-C₃N₄ and the AgBr and ZnO nanoparticles in the g-C₃N₄/AgBr and g-C₃N₄/AgBr/ZnO systems.

3.6. Optical properties

It is well known that the activities of photocatalysts are related to

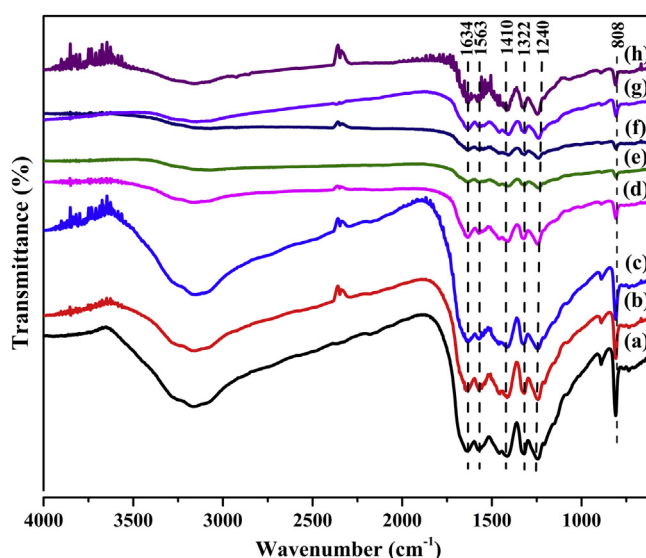


Fig. 7. FTIR spectra obtained for: (a) CN, (b) PCN, (c) CN/AB, (d) CN/AB/ZO 60, (e) CN/AB/ZO 50, (f) CN/AB/ZO 40, (g) CN/AB/ZO 30, and (h) CN/AB/ZO 20.

their optical properties. The UV-Vis DRS results for the samples are shown in Fig. 8a. The attachment of AgBr and ZnO to the surface of g-C₃N₄ enhanced the absorption ability in the visible region of the spectrum. The absorption curve obtained for the ternary nanocomposite g-C₃N₄/AgBr/ZnO exhibited an additional shift toward the visible light spectrum. We plotted $(\alpha h\nu)^2$ versus energy based on the Kubelka–Munk function to determine the optical band gaps for the prepared photocatalysts (Fig. 8b). The DRS results indicated that the band gaps became narrower as the AgBr and ZnO contents were increased [45]. The optical band gaps were determined as 2.68 and 2.41 eV for g-C₃N₄ and CN/AB/ZO 30, respectively. Therefore, the visible light response of g-C₃N₄ was enhanced considerably by coupling to these semiconductors, and thus its photoactivity was better than that of the pure g-C₃N₄.

PL emission spectra can be used to investigate the separation efficiency of photogenerated charges in photocatalysts. As shown in Fig. 9,

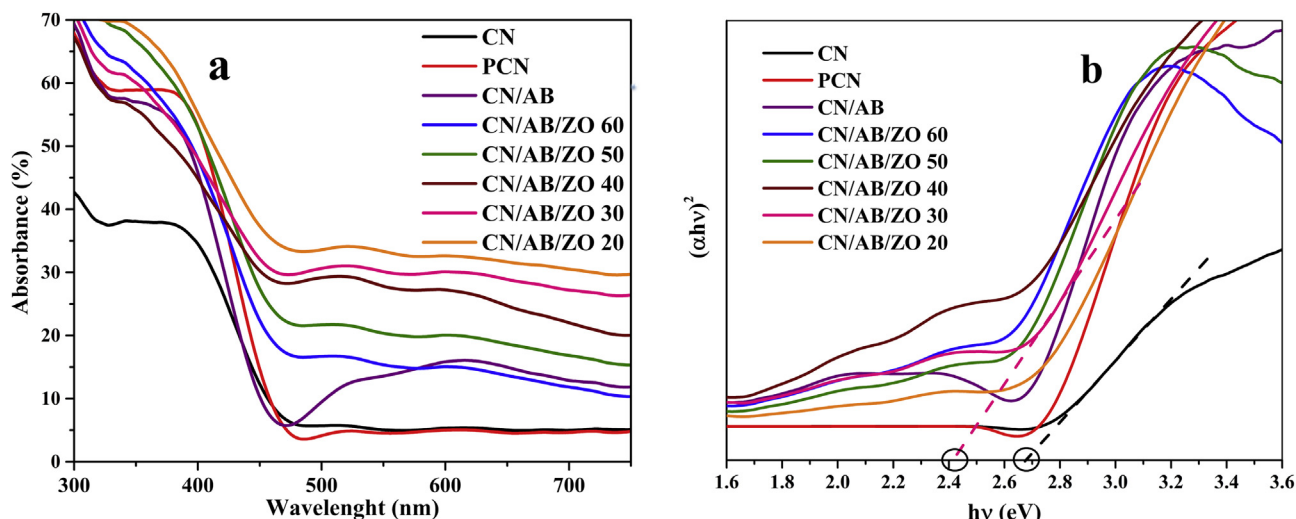


Fig. 8. (a) Diffuse reflectance spectra, and (b) plot of $(\alpha h\nu)^2$ versus $h\nu$ for $g\text{-C}_3\text{N}_4$, $g\text{-C}_3\text{N}_4/\text{AgBr}$, and $g\text{-C}_3\text{N}_4/\text{AgBr}/\text{ZnO}$ photocatalysts.

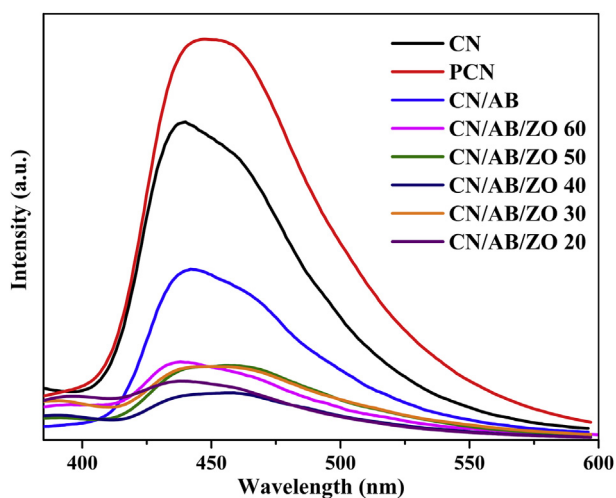


Fig. 9. Room temperature PL spectra obtained for the $g\text{-C}_3\text{N}_4$, $g\text{-C}_3\text{N}_4/\text{AgBr}$, and $g\text{-C}_3\text{N}_4/\text{AgBr}/\text{ZnO}$ photocatalysts when excited at 315 nm.

the bare $g\text{-C}_3\text{N}_4$ had a strong, wide peak in the PL spectrum when excited at 315 nm, whereas the PL emission intensities of the CN/AB and CN/AB/ZO composites decreased remarkably. Hence, the decreased peaks in the PL spectra indicated that fewer excited electrons returned to the ground state, thereby hindering the recombination of electrons and holes in the photocatalysts [46]. Modifications of $g\text{-C}_3\text{N}_4$ with AgBr and ZnO enhanced the separation of electrons and holes to improve its photocatalytic activity under irradiation with visible light.

3.7. Photocatalytic performance

MB was employed to test the photocatalytic performance of the as-prepared photocatalysts under irradiation with visible light. As shown in Fig. 10a, the pure $g\text{-C}_3\text{N}_4$ decomposed 50% of the MB after irradiation with visible light for 80 min. Protonating CN decreased its photodegradation efficiency, thereby demonstrating that protonation only activated the CN to allow its modification with other semiconductors. This lower activity might be explained by the positively charged proton on carbon nitride not adsorbing the cationic dye (MB) as well as CN. After coupling PCN with AgBr, its photocatalytic activity did not change considerably. However, the in situ coupling of PCN with AgBr and ZnO clearly improved its photocatalytic activity, and CN/AB/ZO was an efficient photocatalyst under visible light. Among the different weight

ratios of $g\text{-C}_3\text{N}_4$, $g\text{-C}_3\text{N}_4/\text{AgBr}/\text{ZnO}$ 30 was able to decompose 96.3% of the dye after irradiation for 80 min and it had the highest activity. Its photocatalytic activity was about six times higher than that of the pure $g\text{-C}_3\text{N}_4$. After decreasing the amount of $g\text{-C}_3\text{N}_4$ to 20%, the photodegradation efficiency decreased due to the significant effect of $g\text{-C}_3\text{N}_4$. The reaction kinetics for the as-prepared photocatalysts during the photodegradation of MB followed a pseudo-1st order reaction equation and the kinetic rate constants could be calculated using the following equation: $-\ln(C/C_0) = kt$, where t , k , C , and C_0 are the irradiation time, rate constant, and MB concentrations at time t and 0, respectively (Fig. 10b). The calculated rate constants are listed in Fig. 9b, which shows that the reaction rate was 4.6 times higher than that with the pure $g\text{-C}_3\text{N}_4$. Thus, the heterojunction formed between $g\text{-C}_3\text{N}_4$, AgBr, and ZnO, decreased the recombination of photogenerated electrons and holes. The heterojunction transferred the photogenerated charges much more effectively, and thus the photocatalytic activity of the nanocomposite was highly enhanced under visible light [47]. For comparison, the kinetic rate constants reported in previous studies for MB photodegradation under visible light are shown in Table 2.

3.8. Photocatalytic mechanism

According to the analysis presented above, the synergistic effects of CN/AB/ZO 30 yielded a much better visible light photocatalyst than the pure $g\text{-C}_3\text{N}_4$. These synergistic effects were possibly related to the effective charge transfer at the interface of the semiconductors across the heterojunction, as indicated by the TEM images and XRD patterns, and the appropriate VB and CB positions also facilitated this charge transfer. After exposure to visible light at < 515 nm (as shown by the UV-Vis DRS spectra) with CN/AB/ZO 30, the electrons in the VBs of $g\text{-C}_3\text{N}_4$ and AgBr were excited to the CBs, thereby generating VB holes (h^+) and CB electrons (e^-). However, the band gap of ZnO was too wide to absorb visible light and generate electrons and holes. As a more direct analysis, we evaluated the potentials of the CB and VB edges for $g\text{-C}_3\text{N}_4$, AgBr, and ZnO based on Mulliken electronegativity theory [38]. CB and VB were estimated as -1.10 and $+1.58$ eV for $g\text{-C}_3\text{N}_4$, respectively, the CB and VB potentials for AgBr were calculated as $+0.06$ and $+2.56$ eV, and the CB and VB for ZnO were predicted as -0.415 and $+2.615$ [52,53]. The predicted band gap positions suggest that the photo-excited electrons in the CB of $g\text{-C}_3\text{N}_4$ can transfer to the CBs of AgBr and ZnO, which are less negative than that of $g\text{-C}_3\text{N}_4$, and the photo-generated holes in the VB of AgBr will migrate to the VB of $g\text{-C}_3\text{N}_4$, which is more negative than that of silver bromide. However, this prediction might not be correct because the standard potential of

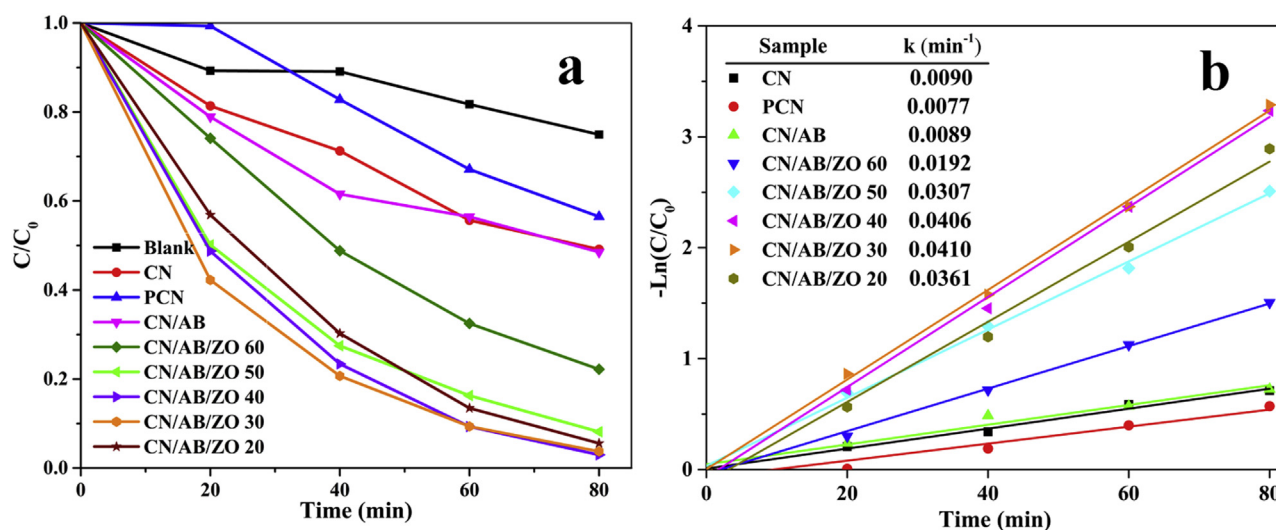


Fig. 10. (a) Photocatalytic performance, and (b) reaction kinetics of the as-prepared samples during MB photodegradation.

Table 2

Comparison of the rate constants during MB visible light photodegradation with the photocatalyst developed in the present study and other g-C₃N₄ based photocatalysts.

Photocatalyst	Degradation rate	Rate constant (min ⁻¹)	Reference
g-C ₃ N ₄ /WO ₃	97% (3 h)	0.0232	[48]
g-C ₃ N ₄ /ZnWO ₄	94% (3 h)	0.0154	[49]
g-C ₃ N ₄ /BiVO ₄	90% (2 h)	0.0178	[50]
g-C ₃ N ₄ /ZnO	37% (2.5 h)	0.0030	[51]
g-C ₃ N ₄ /AgBr/ZnO	96.3% (80min)	0.0410	This work

O₂^{•-}/O₂²⁻ is -0.33 eV [54], which is more negative than the CB potential of AgBr and it is not able to reduce oxygen. In addition, the VBs for both AgBr and g-C₃N₄ are less positive than +2.8 eV [55–57], so they have the ability to oxidize [•]OH into hydroxyl radicals, and thus [•]OH species play a less important role in the photocatalytic reaction, which is consistent with the scavenger experiments discussed in the following. As a consequence, we propose a Z-scheme mechanism for the photodegradation of MB by CN/AB/ZO 30, as shown in Fig. 8 [58–61]. According to the Z-scheme mechanism, photo-excited electrons in the CB of AgBr join the holes in the VB of g-C₃N₄, which gives a greater reducibility potential to the electrons in the CB of g-C₃N₄ to reduce O₂ to [•]O₂⁻ and to react with MB to cause its photodegradation. In addition, some photogenerated electrons transfer from the CB potential of g-C₃N₄ to the CB of ZnO, and because its potential is more negative than -0.33, the transferred electrons in the CB of ZnO can reduce oxygen to the superoxide radical, thereby leading to the photocatalytic degradation of MB. To further understand this process, we conducted experiments to identify the reactive species involved with the photodegradation of MB. EDTA, argon gas, and isopropanol were selected to act as hole (h⁺), superoxide radical ([•]O₂⁻), and hydroxyl radical ([•]OH) scavengers, respectively. As shown in Fig. 11, the addition of isopropanol had no significant effects on the photodegradation of MB by CN/AB/ZO 30, and thus [•]OH was not involved in the process. Moreover, according to the O₂ reduction route ([•]O₂⁻ + 2H⁺ + 2e⁻ → H₂O₂ → 2[•]OH) [62], the pH of the solution should be increased by the production of hydroxyl radicals. However, final pH of the MB solution was the same as the initial pH at 4.5 after irradiation under visible light for 80 min, thereby demonstrating that [•]OH played no significant role in the photodegradation process with CN/AB/ZO 30. By contrast, the addition of EDTA considerably reduced the degradation of MB by the photocatalyst, which shows that h⁺ played a major role. In addition, argon gas decreased the photocatalytic degradation of MB to some

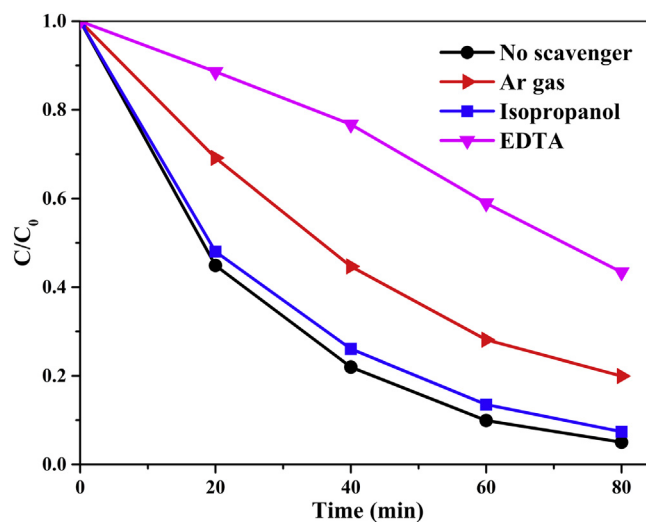


Fig. 11. Photocatalytic degradation of MB by CN/AB/ZO 30 in the presence of EDTA, argon gas, and isopropanol under irradiation with visible light.

extent, thereby indicating that [•]O₂⁻ affected the photodegradation system, but its effect was less than that of h⁺. In fact, the photo-induced electrons could reduce O₂ to [•]O₂⁻, which affected the degradation of MB and the photo-induced holes in the VB of g-C₃N₄ oxidized the MB directly.

The final products obtained by photodegradation are also important, which we determined based on the changes in the UV-Vis absorption spectrum for the MB solution during irradiation with visible light. As shown in Fig. 12, the absorption spectrum obtained for MB became weaker during irradiation but the λ_{max} at 665 nm did not shift at all, which implies that MB was completely mineralized with no intermediate products. Another important issue that affects the photodegradation of dyes is the possible photosensitization of the photocatalyst by the dye. Thus, the changes in the absorption spectrum obtained for MB were used to determine whether the degradation of MB was caused by the photocatalytic activity of the photocatalyst or due to its photosensitization on the photocatalyst's surface [37]. We found no changes in the shape and λ_{max} for the MB solution during photodegradation, and thus we can conclude that MB photosensitization did not occur.

In addition, we determined whether the degradation of MB was due to the photocatalytic activity of the photocatalyst or MB

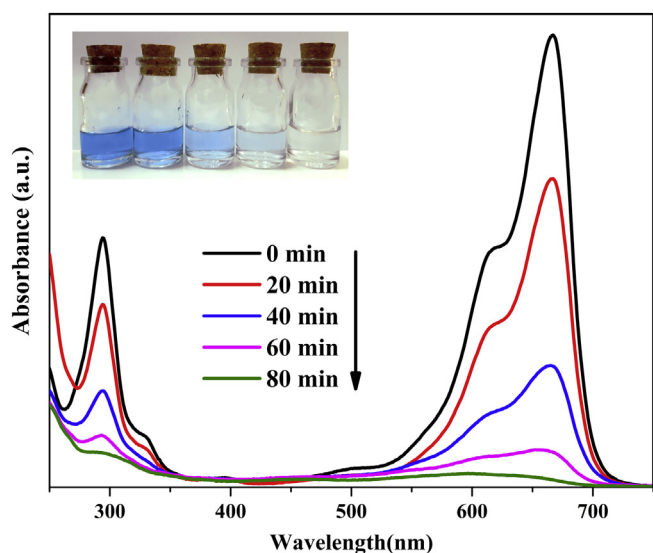


Fig. 12. Changes in the absorption spectrum obtained for MB during its photocatalytic degradation by CN/AB/ZO 30.

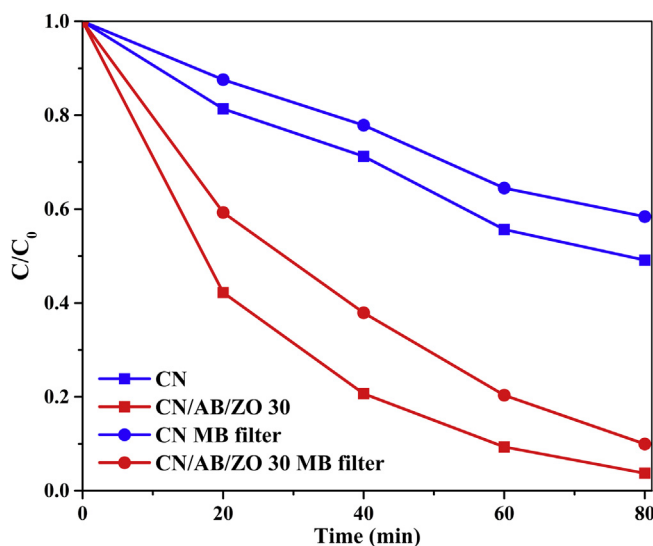


Fig. 13. Photodegradation of MB in the presence of a MB filter using CN and CN/AB/ZO 30, and the results obtained in the normal process without the MB filter.

photosensitization. A MB filter was placed on the beaker containing the photocatalyst and MB solution irradiated under visible light in order to absorb the maximum wavelength related to MB (665 nm), which prevented the excitation of the solution in the beaker so photosensitization could not occur. Thus, any photodegradation of MB in this experiment was due to the pure photocatalytic activity of the photocatalyst. As shown in Fig. 13, the photodegradation of MB with both $g\text{-C}_3\text{N}_4$ and CN/AB/ZO 30 decreased slightly, thereby demonstrating that MB photosensitization affected the process, but the photocatalytic activity of the photocatalyst had the main role in the system.

Fig. 14 shows the proposed mechanism for the photocatalytic degradation of MB under visible light according to the results of the scavenger experiments. All the possible MB degradation routes are illustrated, where one or several could be important.

Another factor that affects the photodegradation of dyes is the surface charge on the photocatalyst, which we determined using zeta potential measurements. As shown in Table 3, the surface of CN/AB/ZO 30 was much more negatively charged, with an average zeta potential

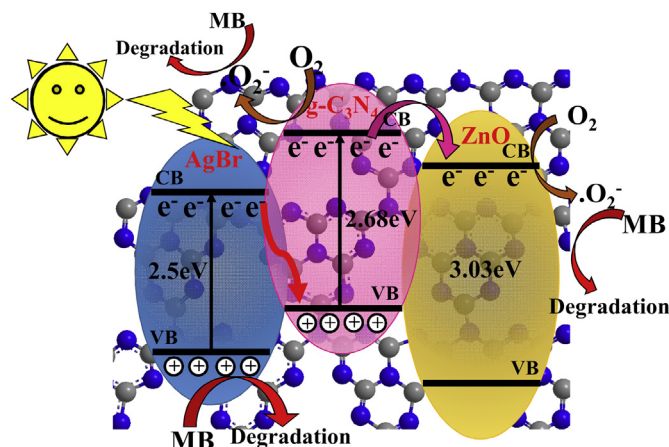


Fig. 14. Schematic illustration of the proposed mechanism for the photocatalytic degradation of MB under irradiation by visible light with $g\text{-C}_3\text{N}_4/\text{AgBr}/\text{ZnO}$.

Table 3

Zeta potential values for the photocatalysts.

Sample	Zeta potential values (mV)
$g\text{-C}_3\text{N}_4$	-532
CN/AB/ZO 30	-1037

value of about -1037 mV compared with -532 mV for $g\text{-C}_3\text{N}_4$. This negative charge may help the novel photocatalyst to make contact with the cationic MB due to the electronic attraction between the negative photocatalyst and the positive dye, thereby improving its photodegradation efficiency.

3.9. Reusability and sustainability

A critical factor that affects the applications of a photocatalyst is its capacity to be reused several times without loss of efficiency. The photocatalyst was tested for cycles to verify its reusability. After each cycle, the remaining photocatalyst was centrifuged, washed with distilled water and ethanol, and dried before the next run. As shown in Fig. 15a, after four cycles, the photocatalyst could still decompose 84.2% of the MB, which is a good performance level for a photocatalyst. In addition, the XRD patterns were compared before and after MB photodegradation to assess the sustainability of the photocatalyst. As shown in Fig. 15b, the XRD patterns were the same and all of the diffraction indexes were at exactly the same degree, although with a slightly lower intensity due to the reduced crystallinity of the photocatalyst after the irradiation process.

4. Conclusion

In this study, we fabricated a ternary $g\text{-C}_3\text{N}_4/\text{AgBr}/\text{ZnO}$ nanocomposite via a sonication-assisted deposition-precipitation technique. After coupling $g\text{-C}_3\text{N}_4$ with two semiconductors comprising AgBr and ZnO, we obtained a highly active ternary photocatalyst under visible light illumination, where its photocatalytic activity was much better compared with that of the pure $g\text{-C}_3\text{N}_4$. Among the different $g\text{-C}_3\text{N}_4$ contents, CN/AB/ZO 30 had the highest activity. This excellent photocatalytic activity was attributed to the synergistic effects and charge transfer between $g\text{-C}_3\text{N}_4$, AgBr, and ZnO, which we attributed to the well-matched band structures of the semiconductors that inhibited electron-hole recombination. We showed that h^+ and $\cdot\text{O}_2^-$ played key roles in the decomposition of MB. Thus, in this study, we developed a feasible method for fabricating a novel heterojunction photocatalyst to remove pollutants from water. However, other types of heterojunctions

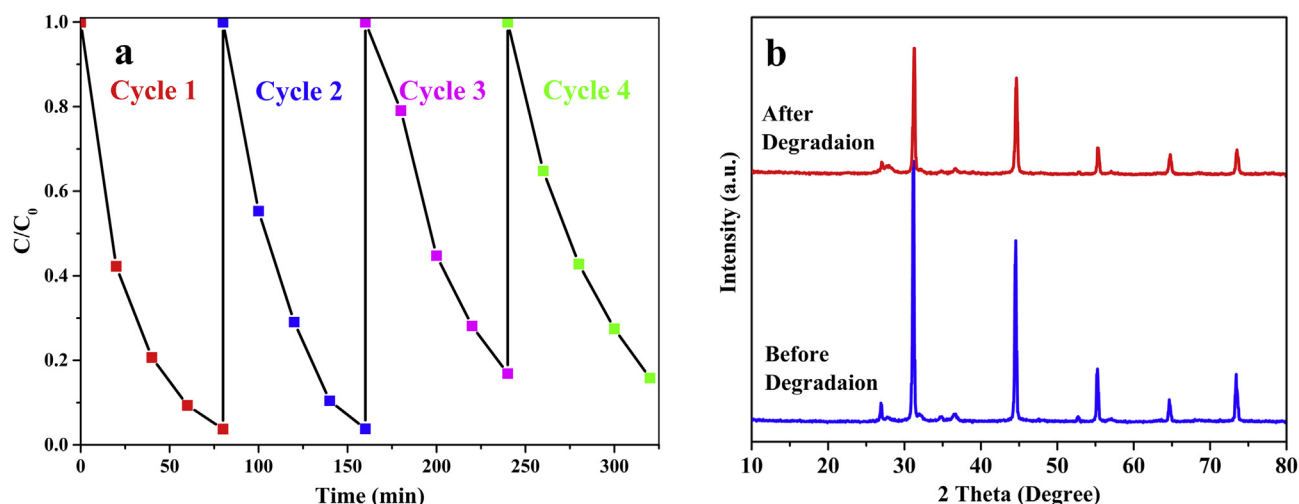


Fig. 15. (a) Reusability test with CN/AB/ZO 30 during the photodegradation of MB under visible light. (b) XRD patterns obtained for CN/AB/ZO 30 before and after MB photodegradation.

may help to degrade pollutants better, so further research is required.

Acknowledgments

This study was financially supported by the University of Tehran.

Appendix A. Supplementary data

Supplementary data related to this article can be found at <http://dx.doi.org/10.1016/j.jpccs.2018.06.024>.

References

- [1] A. Kudo, Y. Miseki, Heterogeneous photocatalyst materials for water splitting, *Chem. Soc. Rev.* 38 (2009) 253–278.
- [2] L. Di, H. Yang, T. Xian, X. Chen, Enhanced photocatalytic activity of NaBH_4 reduced BiFeO_3 nanoparticles for rhodamine B decolorization, *Materials* 10 (2017) 1118.
- [3] C. Zheng, H. Yang, Z. Cui, H. Zhang, X. Wang, A novel $\text{Bi}_4\text{Ti}_3\text{O}_{12}/\text{Ag}_3\text{PO}_4$ heterojunction photocatalyst with enhanced photocatalytic performance, *Nanoscale Res. Lett.* 12 (2017) 608.
- [4] F. Wang, H. Yang, Y. Zhang, Enhanced photocatalytic performance of CuBi_2O_4 particles decorated with Ag nanowires, *Mater. Sci. Semicond. Process.* 73 (2018) 58–66.
- [5] Z. Cui, H. Yang, X. Zhao, Enhanced photocatalytic performance of g-C₃N₄/Bi₄Ti₃O₁₂ heterojunction nanocomposites, *Mater. Sci. Eng. B* 229 (2018) 160–172.
- [6] M. Ghiyasiyan-Arani, M. Masjedi-Arani, M. Salavati-Niasari, Size controllable synthesis of cobalt vanadate nanostructures with enhanced photocatalytic activity for the degradation of organic dyes, *J. Mol. Catal. Chem.* 425 (2016) 31–42.
- [7] R. Monsef, M. Ghiyasiyan-Arani, M. Salavati-Niasari, Application of ultrasound-aided method for the synthesis of NdVO_4 nano-photocatalyst and investigation of eliminate dye in contaminant water, *Ultrason. Sonochem.* 42 (2018) 201–211.
- [8] X. Wang, K. Maeda, A. Thomas, K. Takanabe, G. Xin, J.M. Carlsson, K. Domen, M. Antonietti, A metal-free polymeric photocatalyst for hydrogen production from water under visible light, *Nat. Mater.* 8 (2009) 76–80.
- [9] D. Jiang, L. Chen, J. Xie, M. Chen, $\text{Ag}_2\text{S}/\text{g-C}_3\text{N}_4$ composite photocatalysts for efficient Pt-free hydrogen production. The co-catalyst function of $\text{Ag}/\text{Ag}_2\text{S}$ formed by simultaneous photodeposition, *Dalton Trans.* 43 (2014) 4878–4885.
- [10] D. Ma, J. Wu, M. Gao, Y. Xin, T. Ma, Y. Sun, Fabrication of Z-scheme g-C₃N₄/RGO/ Bi_2WO_6 photocatalyst with enhanced visible-light photocatalytic activity, *Chem. Eng. J.* 290 (2016) 136–146.
- [11] Y. Li, M.-Q. Wang, S.-J. Bao, S. Lu, M. Xu, D. Long, S. Pu, Tuning and thermal exfoliation graphene-like carbon nitride nanosheets for superior photocatalytic activity, *Ceram. Int.* 42 (2016) 18521–18528.
- [12] D. Xiao, D. Yuan, H. He, J. Lu, Microwave-assisted one-step green synthesis of amino-functionalized fluorescent carbon nitride dots from chitosan, *Luminescence* 28 (2013) 612–615.
- [13] B. Yuan, X. Zou, T. Yan, J. Fei, Z. Chu, Green synthesis of graphitic carbon nitride nanodots using sodium chloride template, *J. Nanoparticle Res.* 18 (2016) 1–8.
- [14] G. Shiravand, A. Badiel, G.M. Ziarani, Carboxyl-rich g-C₃N₄ nanoparticles: synthesis, characterization and their application for selective fluorescence sensing of Hg^{2+} and Fe^{3+} in aqueous media, *Sens. Actuators, B* 242 (2017) 244–252.
- [15] X. Gao, X. Jiao, L. Zhang, W. Zhu, X. Xu, H. Ma, T. Chen, Cosolvent-free nanocasting synthesis of ordered mesoporous g-C₃N₄ and its remarkable photocatalytic activity for methyl orange degradation, *RSC Adv.* 5 (2015) 76963–76972.
- [16] H. Wang, W. He, X.a Dong, H. Wang, F. Dong, In situ FT-IR investigation on the reaction mechanism of visible light photocatalytic NO oxidation with defective g-C₃N₄, *Sci. Bull.* 63 (2018) 117–125.
- [17] W. Cui, J. Li, W. Cen, Y. Sun, S.C. Lee, F. Dong, Steering the interlayer energy barrier and charge flow via bioriented transportation channels in g-C₃N₄: enhanced photocatalysis and reaction mechanism, *J. Catal.* 352 (2017) 351–360.
- [18] J. Li, W. Cui, Y. Sun, Y. Chu, W. Cen, F. Dong, Directional electron delivery via a vertical channel between g-C₃N₄ layers promotes photocatalytic efficiency, *J. Mater. Chem. C* 5 (2017) 9358–9364.
- [19] H. Han, G. Ding, T. Wu, D. Yang, T. Jiang, B. Han, Cu and boron doped carbon nitride for highly selective oxidation of toluene to benzaldehyde, *Molecules* 20 (2015) 12686.
- [20] G. Ding, W. Wang, T. Jiang, B. Han, H. Fan, G. Yang, Highly selective synthesis of phenol from benzene over a vanadium-doped graphitic carbon nitride catalyst, *ChemCatChem* 5 (2013) 192–200.
- [21] J. Jin, Q. Liang, C. Ding, Z. Li, S. Xu, Simultaneous synthesis-immobilization of Ag nanoparticles functionalized 2D g-C₃N₄ nanosheets with improved photocatalytic activity, *J. Alloy. Comp.* 691 (2017) 763–771.
- [22] Y. Wang, H. Li, J. Yao, X. Wang, M. Antonietti, Synthesis of boron doped polymeric carbon nitride solids and their use as metal-free catalysts for aliphatic C-H bond oxidation, *Chem. Sci.* 2 (2011) 446–450.
- [23] D.-H. Lan, H.-T. Wang, L. Chen, C.-T. Au, S.-F. Yin, Phosphorous-modified bulk graphitic carbon nitride: facile preparation and application as an acid-base bifunctional and efficient catalyst for CO₂ cycloaddition with epoxides, *Carbon* 100 (2016) 81–89.
- [24] Y. Wang, Y. Di, M. Antonietti, H. Li, X. Chen, X. Wang, Excellent visible-light photocatalysis of fluorinated polymeric carbon nitride solids, *Chem. Mater.* 22 (2010) 5119–5121.
- [25] H. Yan, H. Yang, TiO₂-g-C₃N₄ composite materials for photocatalytic H₂ evolution under visible light irradiation, *J. Alloy. Comp.* 509 (2011) L26–L29.
- [26] Z. Yang, J. Li, F. Cheng, Z. Chen, X. Dong, BiOBr/protonated graphitic C₃N₄ heterojunctions: intimate interfaces by electrostatic interaction and enhanced photocatalytic activity, *J. Alloy. Comp.* 634 (2015) 215–222.
- [27] L. Xu, J. Xia, H. Xu, J. Qian, J. Yan, L. Wang, K. Wang, H. Li, AgX/graphite-like C₃N₄ (X = Br, I) hybrid materials for photoelectrochemical determination of copper (ii) ion, *Analyst* 138 (2013) 6721–6726.
- [28] Y. Ji, J. Cao, L. Jiang, Y. Zhang, Z. Yi, G-C₃N₄/BiVO₄ composites with enhanced and stable visible light photocatalytic activity, *J. Alloy. Comp.* 590 (2014) 9–14.
- [29] W. Cui, J. Li, F. Dong, Y. Sun, G. Jiang, W. Cen, S.C. Lee, Z. Wu, Highly efficient performance and conversion pathway of photocatalytic NO oxidation on SrO-clusters@amorphous carbon nitride, *Environ. Sci. Technol.* 51 (2017) 10682–10690.
- [30] M. Afshar, A. Badiel, H. Eskandarloo, G. Mohammadi Ziarani, Charge separation by tetrahedron-SrTiO₃/TiO₂ heterojunction as an efficient photocatalyst, *Res. Chem. Intermed.* 42 (2016) 7269–7284.
- [31] H. Eskandarloo, A. Badiel, M.A. Behnadjy, Study of the effect of additives on the photocatalytic degradation of a triphenylmethane dye in the presence of immobilized TiO₂/NiO nanoparticles: artificial neural network modeling, *Ind. Eng. Chem. Res.* 53 (2014) 6881–6895.
- [32] H. Eskandarloo, A. Badiel, M.A. Behnadjy, M. Afshar, Enhanced photocatalytic removal of phenazopyridine by using silver-impregnated SiO₂-TiO₂ nanoparticles: optimization of synthesis variables, *Res. Chem. Intermed.* 41 (2015) 9929–9949.
- [33] H. Eskandarloo, A. Badiel, C. Haug, Enhanced photocatalytic degradation of an azo textile dye by using TiO₂/NiO coupled nanoparticles: optimization of synthesis and operational key factors, *Mater. Sci. Semicond. Process.* 27 (2014) 240–253.
- [34] H. Eskandarloo, M. Hashempour, A. Vicenzo, S. Franz, A. Badiel, M.A. Behnadjy, M. Bestetti, High-temperature stable anatase-type TiO₂ nanotube arrays: a study of the structure-activity relationship, *Appl. Catal., B* 185 (2016) 119–132.
- [35] S. Kumar, A. Baruah, S. Tonda, B. Kumar, V. Shanker, B. Sreedhar, Cost-effective

- and eco-friendly synthesis of novel and stable N-doped ZnO/g-C₃N₄ core-shell nanoparticles with excellent visible-light responsive photocatalysis, *Nanoscale* 6 (2014) 4830–4842.
- [36] Y. Feng, J. Shen, Q. Cai, H. Yang, Q. Shen, The preparation and properties of a g-C₃N₄/AgBr nanocomposite photocatalyst based on protonation pretreatment, *New J. Chem.* 39 (2015) 1132–1138.
- [37] M. Rochkind, S. Pasternak, Y. Paz, Using dyes for evaluating photocatalytic properties: a critical review, *Molecules* 20 (2015) 88.
- [38] H. Xu, J. Yan, Y. Xu, Y. Song, H. Li, J. Xia, C. Huang, H. Wan, Novel visible-light-driven AgX/graphite-like C₃N₄ (X = Br, I) hybrid materials with synergistic photocatalytic activity, *Appl. Catal., B* 129 (2013) 182–193.
- [39] W.-J. Ong, L.-L. Tan, S.-P. Chai, S.-T. Yong, A.R. Mohamed, Surface charge modification via protonation of graphitic carbon nitride (g-C₃N₄) for electrostatic self-assembly construction of 2D/2D reduced graphene oxide (rGO)/g-C₃N₄ nanostructures toward enhanced photocatalytic reduction of carbon dioxide to methane, *Nanomater. Energy* 13 (2015) 757–770.
- [40] C. An, J. Wang, W. Jiang, M. Zhang, X. Ming, S. Wang, Q. Zhang, Strongly visible-light responsive plasmonic shaped AgX: Ag (X = Cl, Br) nanoparticles for reduction of CO₂ to methanol, *Nanoscale* 4 (2012) 5646–5650.
- [41] Z.M. Khoshhesab, M. Sarfaraz, M.A. Asadabad, Preparation of ZnO nanostructures by chemical precipitation method, *Synth. React. Inorg. Met. Org. Chem.* 41 (2011) 814–819.
- [42] A.L. Patterson, The Scherrer formula for X-ray particle size determination, *Phys. Rev.* 56 (1939) 978–982.
- [43] Q. Xiang, J. Yu, M. Jaroniec, Preparation and Enhanced visible-light photocatalytic H₂-production activity of graphene/C₃N₄ composites, *J. Phys. Chem. C* 115 (2011) 7355–7363.
- [44] L. Liu, D. Ma, H. Zheng, X. Li, M. Cheng, X. Bao, Synthesis and characterization of microporous carbon nitride, *Microporous Mesoporous Mater.* 110 (2008) 216–222.
- [45] H. Eskandarloo, A. Badiei, M.A. Behnajady, G.M. Ziarani, Ultrasonic-assisted degradation of phenazopyridine with a combination of Sm-doped ZnO nanoparticles and inorganic oxidants, *Ultrason. Sonochem.* 28 (2016) 169–177.
- [46] M. Ou, Q. Zhong, S. Zhang, Synthesis and characterization of g-C₃N₄/BiVO₄ composite photocatalysts with improved visible-light-driven photocatalytic performance, *J. Sol. Gel Sci. Technol.* 72 (2014) 443–454.
- [47] H. Eskandarloo, A. Badiei, M.A. Behnajady, TiO₂/CeO₂ hybrid photocatalyst with enhanced photocatalytic activity: optimization of synthesis variables, *Ind. Eng. Chem. Res.* 53 (2014) 7847–7855.
- [48] L. Huang, H. Xu, Y. Li, H. Li, X. Cheng, J. Xia, Y. Xu, G. Cai, Visible-light-induced WO₃/g-C₃N₄ composites with enhanced photocatalytic activity, *Dalton Trans.* 42 (2013) 8606–8616.
- [49] L. Sun, X. Zhao, C.-J. Jia, Y. Zhou, X. Cheng, P. Li, L. Liu, W. Fan, Enhanced visible-light photocatalytic activity of g-C₃N₄-ZnWO₄ by fabricating a heterojunction: investigation based on experimental and theoretical studies, *J. Mater. Chem.* 22 (2012) 23428–23438.
- [50] Y. Tian, B. Chang, Z. Yang, B. Zhou, F. Xi, X. Dong, Graphitic carbon nitride-BiVO₄ heterojunctions: simple hydrothermal synthesis and high photocatalytic performances, *RSC Adv.* 4 (2014) 4187–4193.
- [51] D. Chen, K. Wang, T. Ren, H. Ding, Y. Zhu, Synthesis and characterization of the ZnO/mpg-C₃N₄ heterojunction photocatalyst with enhanced visible light photocatalytic activity, *Dalton Trans.* 43 (2014) 13105–13114.
- [52] D. Channei, B. Inceesungvorn, N. Wetchakun, S. Ukritnukun, A. Nattestad, J. Chen, S. Phanichphant, Photocatalytic degradation of methyl orange by CeO(2) and Fe-doped CeO(2) films under visible light irradiation, *Sci. Rep.* 4 (2014) 5757.
- [53] W. Liang, G. Tang, H. Zhang, C. Li, H. Li, H. Tang, Core-shell structured AgBr incorporated g-C₃N₄ nanocomposites with enhanced photocatalytic activity and stability, *Mater. Technol.* 32 (2017) 675–685.
- [54] P.M. Wood, The redox potential of the system oxygen—superoxide, *FEBS Lett.* 44 (1974) 22–24.
- [55] W. Yu, J. Chen, T. Shang, L. Chen, L. Gu, T. Peng, Direct Z-scheme g-C₃N₄/WO₃ photocatalyst with atomically defined junction for H₂ production, *Appl. Catal., B* 219 (2017) 693–704.
- [56] W. Yu, D. Xu, T. Peng, Enhanced photocatalytic activity of g-C₃N₄ for selective CO₂ reduction to CH₃OH via facile coupling of ZnO: a direct Z-scheme mechanism, *J. Mater. Chem.* 3 (2015) 19936–19947.
- [57] T. Di, B. Zhu, B. Cheng, J. Yu, J. Xu, A direct Z-scheme g-C₃N₄/SnS₂ photocatalyst with superior visible-light CO₂ reduction performance, *J. Catal.* 352 (2017) 532–541.
- [58] J. Fu, J. Yu, C. Jiang, B. Cheng, g-C₃N₄-based heterostructured photocatalysts, *Adv. Energy Mater.* 8 (2018) 1701503.
- [59] Y. Fu, Z. Li, Q. Liu, X. Yang, H. Tang, Construction of carbon nitride and MoS₂ quantum dot 2D/0D hybrid photocatalyst: direct Z-scheme mechanism for improved photocatalytic activity, *Chin. J. Catal.* 38 (2017) 2160–2170.
- [60] J. Yu, S. Wang, J. Low, W. Xiao, Enhanced photocatalytic performance of direct Z-scheme g-C₃N₄-TiO₂ photocatalysts for the decomposition of formaldehyde in air, *Phys. Chem. Chem. Phys.* 15 (2013) 16883–16890.
- [61] B. Zhu, P. Xia, Y. Li, W. Ho, J. Yu, Fabrication and photocatalytic activity enhanced mechanism of direct Z-scheme g-C₃N₄/Ag₂WO₄ photocatalyst, *Appl. Surf. Sci.* 391 (2017) 175–183.
- [62] J. Jiang, H. Li, L. Zhang, New insight into daylight photocatalysis of AgBr@Ag: synergistic effect between semiconductor photocatalysis and plasmonic photocatalysis, *Chem. Eur. J.* 18 (2012) 6360–6369.